

# Optimizing Laser Ablation of Stainless Steels for Volume Removal and Surface Quality Using Burst of Pulses

Dirk Obergfell,\* Bahman Azarhoushang, and Andrés Fabián Lasagni

Stainless steel alloys are widely used in industrial applications requiring high corrosion resistance and mechanical strength. In many of these applications, laser-based surface processing is utilized for modification, enhancement, or functionalization of the material. However, laser processing is strongly influenced by the alloy's chemical composition, thermal diffusivity, and microstructural characteristics. This study examines the ablation efficiency and surface quality of ablated volumes in AISI 304, AISI 420, and AISI 316Ti steel alloys under ultrashort pulsed laser (250 fs) at various fluence levels and burst configurations (MHz, GHz, and Bi-burst). Key performance parameters, including ablation rate, surface roughness ( $S_a$ ), structure isotropy, and morphology are evaluated using optical, confocal, and scanning electron microscopy methods. The results indicate that MHz bursts substantially enhance ablation rates (e.g., from 1.5 to 3.2 mm<sup>3</sup> min<sup>-1</sup> at 9 J cm<sup>-2</sup>) and ablation energy efficiency (e.g., from  $\approx 1.4$  to 2.75  $\mu\text{m}^3 \mu\text{J}^{-1}$  at 9 J cm<sup>-2</sup>) compared to standard pulsed mode. Furthermore, GHz bursts can achieve superior surface quality ( $S_a \approx 0.5 \mu\text{m}$ ) but with lower ablation rates (0.7 mm<sup>3</sup> min<sup>-1</sup>). Finally, Bi-bursts can balance the performance, reaching moderate ablation rates (3.2 mm<sup>3</sup> min<sup>-1</sup>) with intermediate roughness ( $S_a \approx 2 \mu\text{m}$ ). The results show similar trends across all alloys but highlight AISI 316Ti's susceptibility to microhole formation, which is influenced by the pulse energy distribution.

corrosion resistance, reduced bacterial adhesion, improved surface hardness, and/or enhanced mechanical machinability.<sup>[6–8]</sup>

Given their widespread use and the need for precise fabrication, laser-based processing methods have become essential for shaping and modifying stainless steels with high precision and efficiency. For instance, laser welding and cutting methods, using continuous wave laser sources, have been widely adopted in various industries, including medical and tooling applications, such as gas- and liquid-tight welding of pacemakers or precision cutting of stents.<sup>[9–11]</sup> More recently, laser engraving, marking, and material removal with ultrashort pulsed lasers (USP) have attracted increasing attention due to their flexibility and advantages, including the absence of tool wear, high accuracy, and very low thermal impacts, as evidenced by a reduced heat affected zone compared to nanosecond (ns)-pulsed lasers.<sup>[12–14]</sup>

In this context, time-resolved studies show that in the USP regime, laser–matter interaction proceeds through a sequence of ultrafast, temporally distinct processes.


Initially, the laser energy is absorbed predominantly by the electron system of the material within tens to hundreds of femtoseconds (fs). As a result, the electron temperature rises significantly above that of the crystal lattice, creating a state of strong electron–phonon nonequilibrium.

Additionally, on the picosecond (ps) timescale, energy is transferred from the hot electrons to the colder lattice through electron–phonon coupling. These phenomena typically occur over one to several tens of ps.<sup>[15]</sup>

## 1. Introduction

Stainless steel alloys play a crucial role across a wide range of industries, including medical, food, and tooling sectors.<sup>[1–3]</sup> These materials have superior properties such as excellent biocompatibility, corrosion resistance, and high mechanical strength.<sup>[4,5]</sup> In addition, they are engineered with tailored chemical compositions and microstructure to optimize specific properties, including enhanced

D. Obergfell, A. F. Lasagni  
Institute of Manufacturing  
Technische Universität Dresden  
George-Bähr-Str. 3c, 01069 Dresden, Germany  
E-mail: dirk.obergfell@mailbox.tu-dresden.de

 The ORCID identification number(s) for the author(s) of this article can be found under <https://doi.org/10.1002/adem.202501212>.

© 2025 The Author(s). Advanced Engineering Materials published by Wiley-VCH GmbH. This is an open access article under the terms of the Creative Commons Attribution License, which permits use, distribution and reproduction in any medium, provided the original work is properly cited.

DOI: 10.1002/adem.202501212

D. Obergfell, B. Azarhoushang  
Institute for Advanced Manufacturing (KSF)  
Furtwangen University  
Katharinenstrasse 2, 78532 Tuttlingen, Germany

A. F. Lasagni  
Fraunhofer-Institut für Werkstoff- und Strahltechnik IWS  
Winterbergstr. 28, 01277 Dresden, Germany

An additional contributor to the energy dynamics is thermal transport from the laser-heated surface layer into the bulk of the material. In metals, this occurs primarily via electron heat conduction. These thermal dynamics become especially relevant when considering high repetition rate bursts. Specifically, the temporal spacing between individual pulses in a burst determines how the transient thermal and material states evolve between pulses. In the GHz burst regime, with interpulse delays below 1 ns, subsequent pulses interact with a heated or molten target, promoting cumulative effects because consecutive pulses hit a preheated target. In the MHz regime, where delays exceed 1 ns, the cooling time between pulses is longer but still cumulative effects occur. But this variation in timing can significantly influence both ablation efficiency and resulting surface morphology.<sup>[15]</sup>

Additionally, simulation studies, such as the work by Povarnitsyn et al., showed that delays between double pulses (ps range) significantly affect both energy absorption and crater formation.<sup>[16]</sup> For delays >20 ps plasma shielding effect is observed. This supports the view that even small variations in pulse timing, particularly within a burst, can influence the interaction dynamics by engaging with different stages of the evolving melt and plume.

Further insight into the effects of multipulse ablation are given by Park et al. Time-resolved measurements on GHz burst copper ablation show that the ablation dynamics in this regime depend on the number of GHz burst pulses, irradiation time, and pulse fluence. Whereas single-pulse fs laser ablation generated two types of particles with different ejection speed and at different timescale, GHz ablation leads to an ejection of nanoparticles and ejecta streaks due to recoil pressure on the molten pool by subsequent pulses.<sup>[17]</sup>

Another aspect of multipulse ablation is revealed by Foumani et al. Using a hybrid atomistic-continuum model to study single-pulse ablation of copper, the effect of redeposition of material during double pulse ablation was studied. It was shown that the redeposition of material occurs during double pulse ablation and that it is a dynamic process that strongly depends on the used fluence.<sup>[18]</sup>

From a mechanistic perspective, Chen et al. distinguish between two primary ablation mechanisms in USP processing, spallation and phase explosion. Spallation occurs just above the ablation threshold fluence, where rapid laser-induced electron heating leads to compressive stress in the lattice. Upon relaxation, this transforms into tensile stress that exceeds the material's dynamic strength, causing fracture and ejection of surface layers. In contrast, phase explosion sets in at higher fluences, typically around  $1 \text{ J cm}^{-2}$ , when the lattice becomes deeply superheated near the critical temperature. This leads to the nucleation of vapor bubbles within the melt, resulting in ejection of a liquid-vapor mixture. At sufficiently high fluences, both mechanisms can act simultaneously, resulting in thermodynamic instability in the ablation process.<sup>[19]</sup>

Despite these advances in understanding the physical phenomena, a key challenge remains in achieving optimal removal rates while maintaining high surface quality remains a challenge in USP laser processing.

For instance, while increasing the laser power enhances the removal rate, it also degrades the surface quality of the treated

parts due to overheating, inducing surface and subsurface damage, and finally leading to rougher surfaces.<sup>[20]</sup> With regard to laser-material interactions, different studies have shown that the most effective ablation occurs at fluences ranging from 3 to 15 times the ablation threshold.<sup>[21,22]</sup> Therefore, careful optimization of fluence levels and precise control of laser energy distribution are crucial for controlling both ablation efficiency and surface quality.

A possible solution to this issue is the use of burst of pulses, in which the laser energy is distributed temporally into a train of pulses.<sup>[23]</sup> For instance, Jaeggi et al. reported high ablation rates of up to  $40 \text{ mm}^3 \text{ min}^{-1}$  in copper and brass while preserving moderate surface roughness ( $S_a$ ) through burst mode laser processing.<sup>[24]</sup> In that study, processing was conducted using a polygon scanner operating at a scanning speed of  $\approx 25 \text{ m s}^{-1}$ , with an average power of 243 W and a repetition rate of 5 MHz.

With the use of pulse bursts, two parameters are crucial in influencing both the ablation rate and  $S_a$  of the laser-treated parts. First, the number of bursts per pulse has a significant influence in the ablation process. This approach redistributes a high-energy pulse into a train of lower-energy pulses, maintaining efficiency while enabling higher average power and improved overall performance.<sup>[22,25]</sup> In addition, it has been shown that even when the cumulative fluence of the entire pulse train significantly exceeds the optimal fluence range, the individual pulses contain a lower pulse energy ensuring effective material removal while minimizing waste energy and excess thermal energy.<sup>[26]</sup>

Besides the number of bursts per pulse, the second parameter that is relevant for controlling ablation rate and surface quality is the pulse-to-pulse separation time. Previous studies have shown that the ablation rate and surface quality can vary significantly depending on the burst frequency used (e.g., MHz and GHz, corresponding to pulse spacing of ns and ps, respectively).<sup>[24,27–33]</sup> Bursts in MHz repetition rate can enhance ablation efficiency by taking advantage of heat accumulation, which induces a positive incubation effect.<sup>[30]</sup> However, increasing the intraburst repetition frequency to the GHz range shortens the time between pulses to less than the plasma plume's lifetime. This can lead to ablation plume shielding, hindering the process and reducing efficiency.<sup>[34,35]</sup> Shielding effects vary with fluence in the USP regime. At lower fluences, the ablation plume is dominated by vapor, clusters, and nanoparticles, resulting in minimal optical shielding. In contrast, at higher fluences of around ten times the ablation threshold plasma formation becomes a significant factor, contributing notably to energy shielding and altering subsequent pulse absorption. This transition also affects the plume dynamics and material ejection behavior. The increased plasma density can reduce ablation efficiency by partially reflecting or absorbing incoming laser energy. Moreover, the temporal evolution of the plume becomes critical, especially in burst modes, where subsequent pulses interact with the residual plume and plasma.<sup>[36]</sup>

On the other hand, increased heat accumulation can cause the remelting of a thin surface layer, resulting in reduced  $S_a$ .<sup>[37]</sup> Furthermore, MHz and GHz burst can be combined to Bi-bursts, that have also shown advantages in surface polishing and enhancing ablation efficiency.<sup>[33,38]</sup>

Based on the state of the art, there is a lack in studies on volume ablation using USP lasers, particularly regarding the effects of different burst parameters. While differences of standard pulsed mode and burst mode has been extensively studied on single point laser ablation in previous research, the transferability of those results on burst mode processing of large-scale volume removal remains unclear.<sup>[38,39]</sup> Furthermore, it has not yet been determined whether results from standard pulsed experiments can predict outcomes for burst mode volume ablation. Additionally, the variations in chemical composition, microstructure, and thermal properties among stainless steel alloys may also affect laser processing. Variations in chemical composition can significantly influence the process through differences in the local optical absorption, susceptibility to oxide formation, and differences in the vaporization threshold, all of which might affect energy coupling.<sup>[6–8]</sup> Changes in microstructure such as grain size, phase distribution, or crystallographic orientation can also affect the local thermal conductivity, leading to differences in heat flow. Additionally, local variations in thermal properties like heat capacity and thermal diffusivity impact heat accumulation and dissipation, thereby modifying melting dynamics and ablation thresholds.

As estimated by formulas such as those from Bauer et al., steels with low thermal conductivity accumulate more heat and reach higher surface temperatures under identical laser conditions, resulting in stronger melt effects, whereas high thermal conductivity steels dissipate heat more efficiently, leading to lower temperature buildup.<sup>[40]</sup> The differing material properties also result in varying ablation thresholds, which were previously found to be  $\approx 0.3 \text{ J cm}^{-2}$  for 316Ti and 304 steels, and about  $0.25 \text{ J cm}^{-2}$  for 420 steel for single-pulse ablation.<sup>[38]</sup> This study examines the impact of various burst parameters on volume ablation and surface quality in three stainless steel alloys, namely AISI 420, AISI 304, and AISI 316Ti, which have been selected due to their different thermal properties, such as thermal conductivity and specific heat capacity. To isolate the effects of laser fluence and burst parameters on material removal and surface characteristics, different fluence regimes are explored while maintaining a constant pulse duration.

Laser processing using burst modes has been widely investigated. While some studies have focused on long burst sequences involving more than 100 pulses per burst, others have explored short-burst regimes such as MHz, GHz, and Bi-bursts to study ablation mechanisms in various materials.<sup>[31–33,41–47]</sup> Förster et al. presented a comprehensive review of burst processes, highlighting that ablation efficiency can be enhanced in both

the MHz and GHz regimes. However, the degree of improvement is highly dependent on the material that is used and the specific application, such as drilling or milling.<sup>[41]</sup>

This study specifically focuses on short-burst sequences consisting of 3 to 10 pulses per burst, with the objective of operating within the optimal fluence range for stainless steel processing. To the best of our knowledge, there is no prior study that systematically compares ablation rate, ablation efficiency, and surface quality across different stainless steel alloys under such burst mode conditions. The treated surfaces are characterized using confocal microscopy, scanning electron microscopy as well as optical microscopy, for determining  $S_a$  parameters, isotropy as well as the presence of defects.

## 2. Experimental Section

### 2.1. Materials

For the structuring experiments, 1 mm thick stainless steel samples (HSM Stahl- und Metallhandel, Germany) of AISI 304 (X5CrNi18-10), AISI 420 (X46Cr13), and AISI 316Ti (X6CrNiMoTi1) alloys were used. The metallic sheets were cut to  $100 \times 100 \text{ mm}$  samples. These alloys were of special interest due to their importance within the medical industry and were selected of their significantly different thermal diffusivities, which might affect their ablation behavior. The diffusivities together with the used material properties are listed in **Table 1**. For instance, it can be seen that the thermal diffusivity of the AISI 420 steel was significantly higher ( $\approx 2.4$  times) compared to both AISI 304 and 316Ti steels. Furthermore, there are differences in the microstructure and crystal structure of the materials: AISI 420 is a martensitic steel, while AISI 304 and AISI 316Ti are austenitic steels, which might also affect the laser processing. The electron–phonon coupling strength, can vary significantly between different crystal structures such as face-centered cubic (FCC) and body-centered tetragonal. In general, stronger coupling leads to more rapid lattice heating and consequently lower ablation thresholds during ultrafast laser processing.<sup>[48,49]</sup> In addition, thermal conductivity and diffusivity which is typically higher and more isotropic in FCC metals, play a critical role in determining the rate at which deposited energy disperses from the irradiated region. These properties directly affect heat accumulation and melting dynamics, particularly under burst mode laser conditions where interpulse thermal effects are pronounced.<sup>[15]</sup> Furthermore, the mechanical response of the lattice, including properties like yield strength and the propensity for plastic deformation, also depends

**Table 1.** Material properties of the used stainless steel alloys in this study (extracted from the manufacturer data sheets).

Material type	Chemical composition	Thermal conductivity $k$ [ $\text{W m}^{-1} \text{K}^{-1}$ ]	Specific heat capacity $c$ [ $\text{J kg}^{-1} \text{K}^{-1}$ ]	Density $\rho$ [ $\text{kg m}^{-3}$ ]	Thermal diffusivity $\alpha$ [ $\text{m}^2 \text{s}^{-1}$ ]
AISI 420	C 0.50%, Si $\leq 1.00\%$ , Mn $\leq 1.00\%$ , P $\leq 0.040\%$ , S $\leq 0.015\%$ , Cr 14.50%, Mo $\leq 0.50\%$	30	460	7700	$8.47 \times 10^{-6}$
AISI 304	C $\leq 0.07\%$ , Si $\leq 1.00\%$ , Mn $\leq 2.00\%$ , P $\leq 0.045\%$ , S $\leq 0.03\%$ , Cr 19.50%, Ni 10.50%, N $\leq 0.11\%$	15	500	7900	$3.80 \times 10^{-6}$
AISI 316Ti	C $\leq 0.08\%$ , Si $\leq 1.00\%$ , Mn $\leq 2.00\%$ , P $\leq 0.04\%$ , S $\leq 0.03\%$ , Cr 18.50%, Ni 13.50%, Mo 2.50%, Ti 0.70%	15	500	8000	$3.75 \times 10^{-6}$

on the underlying crystal structure. Such mechanical characteristics influence ablation mechanisms such as stress confinement and spallation, contributing to material-specific laser response behaviors.<sup>[50]</sup> After the laser process, the samples were stored under atmospheric conditions and without any other additional treatment.

## 2.2. Laser Ablation Treatment

The laser processing was carried out using a five-axis laser workstation (GFMS LP400u, Switzerland). The system was equipped with a solid-state USP laser source (Light Conversion Carbide CB-3, Lithuania), which emits a fundamental wavelength of 1030 nm. The burst of pulses was generated by splitting the main pulse into sub-pulses in the MHz and GHz range. The laser had a maximum average power of 40 W with a maximal pulse energy  $E_p$  of 200  $\mu$ J. The laser beam was deflected on the surface using a galvanometer scanner (Scanlab Excelliscan, Germany) equipped with an f-theta lens having a focal distance of 160 mm. This optical setup led to a beam diameter  $\omega_0$  of  $\approx 38 \mu$ m. The process parameters were selected based on prior optimization studies aiming to achieve high ablation speed while maintaining good surface quality. Research demonstrated that a relatively high pulse overlap ( $\approx 90\%$ ) in combination with high scanning speeds resulted in superior surface finish.<sup>[51]</sup> In addition, short pulse durations were shown to enhance ablation efficiency.<sup>[38]</sup> Consequently, a pulse duration of 250 fs was chosen for this study.

The value of the applied laser fluence  $\phi_{av}$  can be then calculated using Equation (1)

$$\phi_{av} = \frac{4 E_p}{\pi \omega_0^2} \quad (1)$$

where  $E_p$  is the pulse energy.

Different burst parameters were tested using pulse durations of 250 fs and compared with the same laser parameters without using burst mode (single-pulse experiments). For the ablation tests,  $2 \times 2$  mm cavities were created with 150 slices for each laser parameter. The scanning speed was  $3 \text{ m s}^{-1}$  and the repetition rate 200 kHz. The hatch distance was set to  $5 \mu$ m, which leads to an overlap of eight pulses at each spatial position.

The removal rate per applied energy ( $Q'$  [ $\mu\text{m}^3 \mu\text{J}^{-1}$ ]) and per time ( $Q$ ) [ $\text{mm}^3 \text{min}^{-1}$ ] was calculated using the following equations<sup>[25]</sup>

$$Q' = \frac{h P_x P_y f_L}{N_l P_{av}} \quad (2)$$

$$Q = \frac{c_v}{v_{scan} N_l P_{av}} \quad (3)$$

where  $h$  is the step-height (height of the ablated volume),  $P_x$  and  $P_y$  the pulse pitches in  $x$  and  $y$  direction,  $f_L$  repetition rate,  $N_l$  the number of layers,  $N_{sl}$  the number of lines per layer,  $c_v$  trench volume, and  $P_{av}$  the average power. The scan direction was rotated  $79^\circ$  after each layer.

For the burst parameters, GHz, MHz, and Bi-burst modes were used. The Bi-burst mode is defined as a combination of both MHz and GHz bursts. For the GHz burst, the intraburst pulse separation time was 450 ps, corresponding to 2.22 GHz. In case of the MHz burst mode, the intraburst pulse separation time was 17 ns (65 MHz). The pulse energy of the individual sub-pulses in a burst is a fraction of the total energy that would be delivered by a single pulse. For example, when using a three-pulse GHz burst with a total energy equivalent to a 100  $\mu$ J single pulse, each sub-pulse in the burst carried approximately one-third of the energy, that is,  $\approx 33 \mu$ J.

In the case of Bi-burst operation, where both MHz and GHz bursts were combined, the total pulse energy was distributed between the two burst regimes. For instance, with a total energy of 100  $\mu$ J, a three-pulse MHz burst delivered  $\approx 33 \mu$ J per pulse, and each of the subsequent GHz sub-pulses carried a fraction of that (e.g.,  $\approx 11 \mu$ J per pulse in a three-pulse GHz sequence nested within each MHz pulse). To investigate the influence of different burst modes, the number of bursts was varied between 3–10 GHz and 3–10 MHz bursts, and a combination of GHz and MHz bursts (Bi-burst).

**Figure 1** shows representative oscilloscope measurements illustrating the energy distribution for various burst modes. These measurements captured pulses with differing numbers of bursts per pulse and distinct intraburst time delays in the ps and ns ranges, corresponding to GHz and MHz burst modes, respectively, as described before. The oscilloscope traces highlighted how both the number of bursts and the intraburst delay impacted the temporal energy distribution within each pulse. As can be seen, independently of the number of burst or the used repetition rate, the last pulse of the pulse train always had a significant higher energy (almost doubled) than the previous pulses, which seems to be a characteristic of the used laser source. In Bi-burst mode

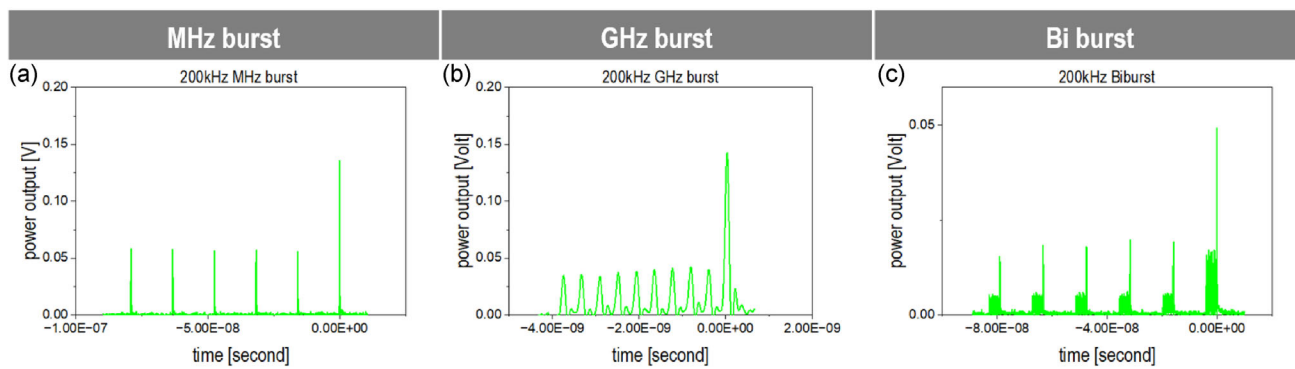


**Figure 1.** a) Oscilloscope measurements of 6 MHz bursts, b) 10 GHz bursts, and c) 6 MHz and 10 GHz bursts combined (Bi-burst).

(Figure 1c), both MHz and GHz were combined. The energy distribution of each burst remained unchanged but the overall intensity was reduced because it was spread over a greater number of pulses. A fast photodiode (InGaAs, EOT-3500) with a rise/fall time of <25 ps was used for signal detection, and measurements were recorded using a high-bandwidth oscilloscope (Keysight MSO-X 6004 A, 6 GHz bandwidth).

### 2.3. Surface Characterization

For analyzing the ablated volume of the produced cavities, a confocal microscope (Keyence VK-3000, Japan) was utilized with a 20x microscope objective with NA 0.46 and lateral resolution of 0.1  $\mu\text{m}$ . The axial resolution was 0.04  $\mu\text{m}$ . Furthermore, scanning electron microscope (SEM) images were taken on selected samples (Crossbeam 550 L Zeiss, Germany) to better evaluate the produced surface topology. The open-source Python software package Surfalize was employed to analyze the depth, volume, and  $S_a$  of the cavities, enabling standardized analysis for a large set of confocal images.<sup>[52]</sup> The isotropy of the SEM images was extracted using the software  $\mu\text{soft}$  analysis (Mountains, France). The isotropy of the SEM images was extracted using the software  $\mu\text{soft}$  analysis (Mountains, France). Isotropy refers to the uniformity of surface characteristics in all in-plane directions. For example, a perfectly flat surface can be considered fully isotropic (isotropy = 100%), exhibiting no directional dependence. In contrast, a brushed surface with a texture oriented along a specific direction is fully anisotropic (isotropy = 0%). Surface quality, particularly regarding defects, was examined with an optical microscope with 100x magnification (Keyence VHX-7000, Japan).

## 3. Results and Discussion

### 3.1. Impact of Burst Parameters on Removal Efficiency, Removal Rate, and Surface Roughness

In the first set of experiments, the effects of different burst modes on the ablation behavior of the three investigated materials were examined. This was done by ablating  $2 \times 2$  mm areas, producing rectangular trenches. The graphs presented in **Figure 2**, for stainless steel type AISI 420, show the impact of MHz (Figure 2a–c), GHz (Figure 2d–f), and Bi-burst (Figure 2g–i) modes, evaluating removal rate ( $\text{mm}^3 \text{min}^{-1}$ ), removal efficiency ( $\mu\text{m}^3 \mu\text{J}^{-1}$ ), and  $S_a$  ( $\mu\text{m}$ ). It is important to note that the y-axis scales vary among the graphs, and this should be taken into account when comparing the data. The corresponding graphs for the alloys AISI 304 and AISI 316Ti are provided in the supplementary material section (see Figure S1 and S2, Supporting Information, respectively).

For MHz bursts, the material removal rates ( $Q$ , calculated using Equation (2)) were notably increased in the high-fluence regime when compared to standard pulsed ablation. Specifically, at a fluence of  $9 \text{ J cm}^{-2}$ , the removed material volume was increased from  $1.5 \text{ mm}^3 \text{min}^{-1}$  in standard pulsed mode to  $3.2 \text{ mm}^3 \text{min}^{-1}$  when ten bursts in the MHz range are used (Figure 2a). At higher fluence levels ( $>9 \text{ J cm}^{-2}$ ), the material removal rate in standard pulsed ablation was lower than in MHz burst ablation, since for the last case heat accumulation within the pulse train can reduce the ablation threshold and lead to higher absorptivity.<sup>[35]</sup> In

addition, the MHz repetition rate leads to a pulse-to-pulse time separation of 17 ns exceeding the lifetime of the plasma plume, which is in the ps range.<sup>[35,42]</sup> Therefore, shielding effects do not occur. Additionally, electron-lattice thermalization occurs within this time frame, transferring energy to the bulk material. This process raises the material's temperature, which enhances the efficiency of the ablation process by facilitating energy absorption and material removal.<sup>[53,54]</sup>

In contrast, GHz bursts permitted achieving a maximum removal rate of  $0.7 \text{ mm}^3 \text{min}^{-1}$  in the best case, at comparable fluence levels (Figure 2d). Notably, regardless of the number of pulses per burst, all burst modes result in a lower removal rate compared to standard pulsed (no burst) ablation. The reduction becomes increasingly pronounced as the laser fluence increases. For example, at  $9 \text{ J cm}^{-2}$ , the removal rate decreased by a factor of four compared to standard pulsed mode, dropping from  $3.2 \text{ mm}^3 \text{min}^{-1}$  to less than  $0.8 \text{ mm}^3 \text{min}^{-1}$ . Furthermore, with Bi-bursts, depending on the specific burst configuration, the removed volume could reach values similar to those observed with no burst, of  $\approx 3.2 \text{ mm}^3 \text{min}^{-1}$  at  $17 \text{ J cm}^{-2}$  (Figure 2g). However, variations within the Bi-burst configuration reveal notable differences. Increasing the proportion of MHz bursts within the pulse train results in higher material removal (e.g., from  $1 \text{ mm}^3 \text{min}^{-1}$  with 3 MHz burst to  $3.2 \text{ mm}^3 \text{min}^{-1}$  with 10 MHz burst at  $17 \text{ J cm}^{-2}$ ), whereas a higher proportion of GHz bursts reduces the removed volume (e.g., from  $1.5 \text{ mm}^3 \text{min}^{-1}$  with 10 GHz burst to  $1 \text{ mm}^3 \text{min}^{-1}$  with 3 GHz burst at  $17 \text{ J cm}^{-2}$ ).

In terms of ablation efficiency ( $Q'$ , calculated using Equation (3)), the results indicate that GHz bursts result in significantly lower performance compared to standard pulsed (no burst) ablation across the tested fluence range (Figure 2e). For instance, at  $3.5 \text{ J cm}^{-2}$ , the GHz burst reached an ablation efficiency of  $1.5 \mu\text{m}^3 \mu\text{J}^{-1}$ , whereas for single pulses it was  $\approx 2.5 \mu\text{m}^3 \mu\text{J}^{-1}$ .

The reason for the negative impact is particle- and plasma shielding that occurs now when using GHz burst, where the intra-burst delay time is 450 ps and therefore it is in the same range as the lifetime of the plasma plume.<sup>[45]</sup> This means that the following pulse within the pulse train can hit the plasma plume of the preceding pulse and therefore a part of the energy is shielded and reflected.<sup>[27]</sup> Similarly, using Bi-burst mode can also lead to a reduction in efficiency, ranging from 20% to 70%, depending on the burst configuration (Figure 2h). For example, using a configuration of 7 MHz and 10 GHz reduces the efficiency from  $\approx 1.5$  (single pulse) to  $0.8 \mu\text{m}^3 \mu\text{J}^{-1}$  (47%) and with 3 MHz and 10 GHz to  $<0.5 \mu\text{m}^3 \mu\text{J}^{-1}$  (67%). The highest efficiency of  $\approx 1.3 \mu\text{m}^3 \mu\text{J}^{-1}$  in Bi-burst mode was reached when using 10 MHz and 10 GHz burst. Notably, the effect of combining the bursts is more efficient, when using a larger number of bursts within the pulse, as the negative effects like plasma and particle shielding are minimized and positive effects like heat accumulation are more pronounced.<sup>[12]</sup>

On the other hand, employing MHz bursts enhances the ablation efficiency in fluence regimes above  $3 \text{ J cm}^{-2}$ , with improvements exceeding 50% (e.g.,  $\approx 1.4$ – $2.75 \mu\text{m}^3 \mu\text{J}^{-1}$  at  $9 \text{ J cm}^{-2}$ , Figure 2b).

Regarding surface quality, quantified by  $S_a$ , standard pulsed ablation (no burst) produces a linear increase in  $S_a$  with increasing fluence (e.g., from  $2 \mu\text{m}$  at low fluence to  $14 \mu\text{m}$  at highest

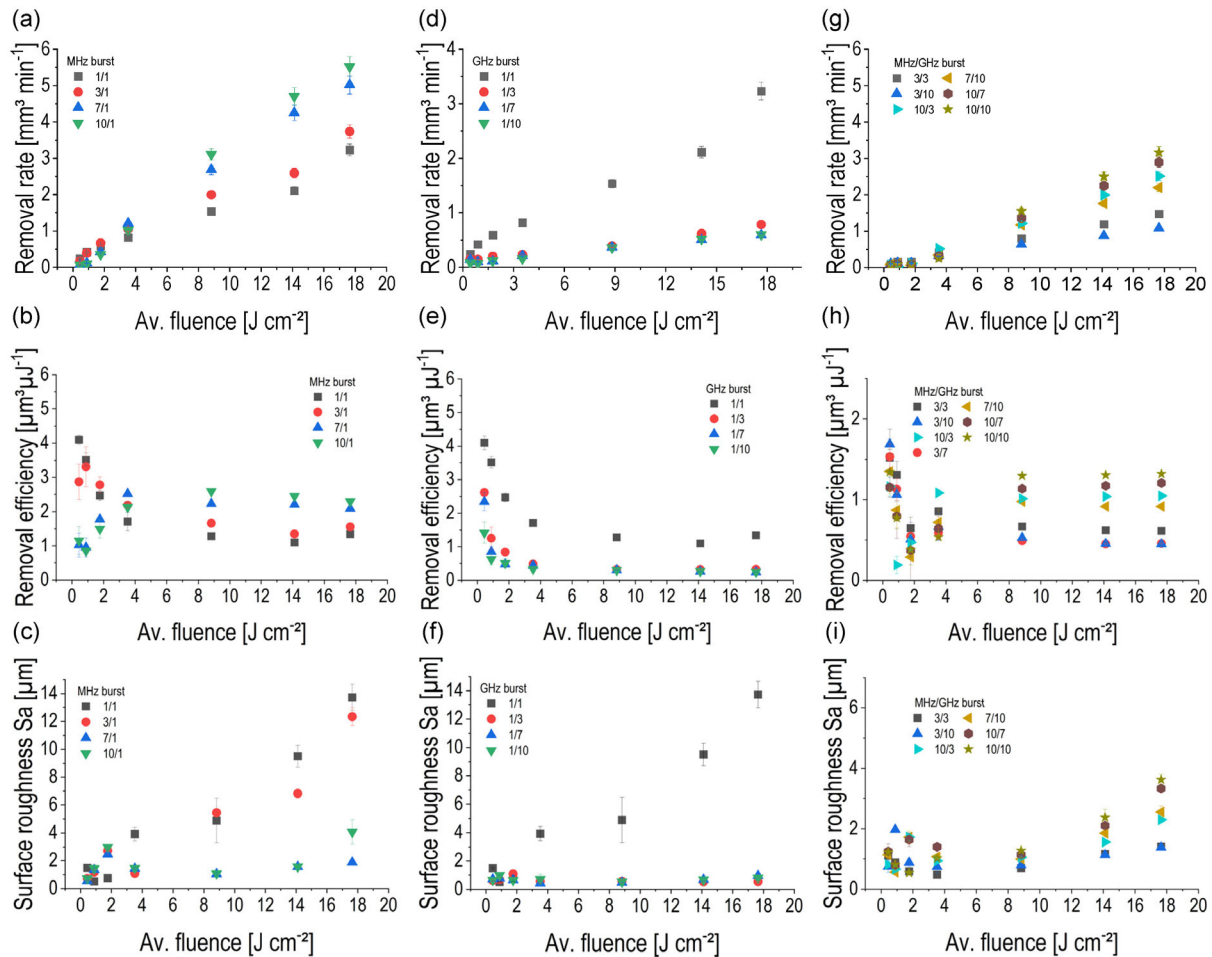


**Figure 2.** a,d,g) Removal rate, b,e,h) removal efficiency, and c,f,i) obtained  $S_a$ , using different burst parameters, obtained in stainless steel type AISI 420 (corresponding graphs for the alloys AISI 304 and AISI 316Ti are provided in the Supporting Information section S1 and S2). The numbers given in the legend (e.g., 1/1, 3/1, and 7/1) denote the ratio of the number of pulses in each burst train for the MHz and GHz pulse types, respectively. For example, a 3/1 ratio indicates that each burst train contains three MHz pulses and one GHz pulse. Error bars indicate the standard deviation over three repeated measurements, reflecting both process variation for specific removal rate and  $S_a$ . In many cases, error bars are present but may not be visible due to their small size.

fluence, see 1/1 labeled data in Figure 2c). However, when burst mode ablation is employed,  $S_a$  exhibits less variation across all fluence levels (Figure 2c,f,i).

The shift of the maximum ablation efficiency peak toward higher average fluences with increasing burst number in the MHz mode is attributed to the decreasing fluence per individual pulse within a burst. For example, in the 10/1 burst mode, each pulse carries less than  $1 \text{ J cm}^{-2}$ , while for 3/1 and 7/1 modes, the per-pulse fluences are  $\approx 0.3 \text{ J cm}^{-2}$  and  $0.5 \text{ J cm}^{-2}$ , respectively. This reduction in per-pulse fluence likely results in cumulative heating and incubation effects that shift the efficiency peak toward higher average fluences.

For MHz bursts (Figure 2c), the  $S_a$  strongly depends on the number of burst. At a burst configuration of three pulses per burst,  $S_a$  also increases with the applied laser fluence, though it remains moderately lower than in the standard pulsed regime, reaching  $\approx 12 \mu\text{m}$  at a fluence of  $17 \text{ J cm}^{-2}$  (labeled with 3/1 in Figure 2c). A clear trend is observed wherein increasing the number of pulses per burst leads to a reduction in  $S_a$  at high

fluence levels. For instance, with ten pulses per burst, the  $S_a$  is significantly reduced to  $\approx 2 \mu\text{m}$  at the same fluence (see labeled with 3/1 data in Figure 2c).

For GHz bursts (Figure 2f), almost no increase of the  $S_a$  with rising fluence could be observed at all GHz burst configurations. Even at high-fluence regime ( $17 \text{ J cm}^{-2}$ ) with all configurations  $S_a$  values below  $1 \mu\text{m}$  were reached. The improved surface quality observed with GHz bursts, compared to MHz bursts, can be attributed to an enhanced heat accumulation, which forms a very thin remolten layer on the material's surface.<sup>[37]</sup>

When using Bi-bursts (Figure 2i), a linear increase in  $S_a$  was observed at higher fluence levels, particularly above  $6 \text{ J cm}^{-2}$ . Despite this, depending on the specific configuration of the Bi-burst mode, lower  $S_a$  values compared to single pulse (no burst) could be achieved (e.g.,  $S_a \approx 1 \mu\text{m}$  at  $9 \text{ J cm}^{-2}$ ). Additionally, the ratio of MHz to GHz bursts was found to influence the  $S_a$ . Specifically, a higher proportion of MHz bursts within the Bi-burst causes a moderate increase in  $S_a$  (from  $1.3$  to  $3.8 \mu\text{m}$ , Figure 2i).  $S_a$  increases with fluence due to the

transition from stress-driven spallation regime to highly dynamic and unstable ablation regimes involving melt flow (phase explosion) which is caused by working far above the ablation threshold. The specific temporal structure of the burst (MHz vs. GHz) determines the amount of heat that is accumulated. Due to the higher heat accumulation in GHz burst mode, melt formation is more likely to occur, allowing surface irregularities generated during ablation to be partially smoothed by the flow and resolidification of the molten material.<sup>[55]</sup> These results from Bi-bursts are consistent with those from pure MHz bursts, indicating that the proportion of MHz pulses in a Bi-burst influences the  $S_a$  in similar manner to using only MHz bursts.<sup>[56,57]</sup> Interestingly, increasing the number of GHz pulses within the Bi-burst leads to a rise in  $S_a$ , contrary to the trend observed when using GHz bursts alone (from  $\approx 2$  to  $3.8 \mu\text{m}$  at  $17 \text{ J cm}^{-2}$ ).

When comparing the results presented in Figure 2 with those of the other stainless steel alloys (AISI 304 and AISI 316Ti, see Figure S1 and S2 in the Supporting Information) that were investigated, it can be observed that the general trends for both materials are similar.

In summary, the ablation performance and surface quality are strongly influenced by the temporal pulse structure. The highest ablation efficiency was achieved using MHz bursts, with a maximum ablation rate of  $5.5 \text{ mm}^3 \text{ min}^{-1}$  observed at a fluence of  $17 \text{ J cm}^{-2}$  under a 10 MHz burst configuration (for AISI 304). A paired t-test has been conducted for MHz and GHz burst. The paired t-test comparing removal rates between MHz and GHz burst modes showed a substantial difference in performance (mean:  $2.13$  vs.  $0.28 \text{ mm}^3 \text{ min}^{-1}$ ). The result was statistically significant under a one-sided hypothesis ( $t(6) = 2.35$ ,  $p = 0.029$ ), indicating that MHz bursts yield higher removal rates. Although the two-sided  $p$ -value ( $0.057$ ) slightly exceeded the  $0.05$  threshold, the extremely high correlation between paired values ( $r = 0.999$ ) supports a consistent fluence-dependent trend favoring MHz over GHz. This increase in efficiency is accompanied by a corresponding rise in  $S_a$ . In contrast, GHz bursts result in significantly improved surface quality (using 3–10 GHz bursts), with  $S_a$  values below  $1 \mu\text{m}$  measured consistently across all tested steels, although the ablation efficiency is comparatively lower. A paired t-test comparing  $S_a$  between the same burst modes revealed a statistically significant difference ( $t(6) = 2.71$ ,  $p = 0.035$ ), with GHz bursts producing smoother and more consistent surfaces (mean  $S_a = 0.72 \mu\text{m}$ ) compared to MHz bursts (mean  $S_a = 1.91 \mu\text{m}$ ). Bi-burst configurations provide an intermediate outcome, with their performance depending on the specific intraburst composition. For all investigated materials, Bi-bursts enabled ablation rates ranging from  $1$  to  $3 \text{ mm}^3 \text{ min}^{-1}$ , along with  $S_a$  values between  $1$  and  $4 \mu\text{m}$ . For efficient ablation, this study demonstrates that MHz burst mode yields the highest material removal efficiency. Specifically, using a 10 MHz burst at a fluence of  $17 \text{ J cm}^{-2}$  achieves in the highest ablation rates while maintaining a  $S_a$  of  $\approx 4 \mu\text{m}$ , which represents an acceptable level for many industrial applications. For applications requiring higher surface quality, a shift to 10 GHz burst mode can further reduce  $S_a$  below  $1 \mu\text{m}$ . Alternatively, Bi-burst mode offers a flexible approach, enabling a tunable balance between ablation rate and surface quality depending on the specific process requirements.

Process optimization in high-power pulsed systems can be achieved by tailoring both temporal beam shaping and the

processing strategy. For example, a combination of roughing by MHz burst and finishing by GHz burst can be used. In addition, other authors reported that spatial beam shaping and beam splitting (multibeam processing) can be beneficial for process optimization.<sup>[41]</sup>

### 3.2. Impact of Burst Parameters on Surface Morphology

To evaluate the influence of laser parameters on surface morphology, SEM imaging was performed for the conditions that produced the highest ablation rates within each burst configuration. **Figure 3** presents SEM images of  $2 \text{ mm} \times 2 \text{ mm}$  rectangular trenches formed in three stainless steel alloys: AISI 420, AISI 304, and AISI 316Ti. Each trench was produced by scanning the target area 150 times, and the used process parameters were kept constant (fluence:  $\approx 17 \text{ J cm}^{-2}$ ; scanning speed:  $3 \text{ m s}^{-1}$ ; pulse duration 250 fs; hatch distance:  $5 \mu\text{m}$ ).

Notably, similar surface morphologies were observed across all alloys treated under the same process parameters.

Significant variations in surface morphology were observed when comparing different used temporal shapes. For standard pulsed mode, the treated surfaces exhibit a rough texture characterized by uniformly distributed, cone-like protrusions across the entire ablation area (Figure 3a–c).

Specifically, MHz bursts result smoother surfaces, as indicated by a reduction in  $S_a$  (see Figure 3d–f). In contrast, with using GHz bursts the resulting surfaces are exceptionally smooth and homogeneous (see Figure 3g–i).

The Bi-burst mode, which combines MHz and GHz sub-bursts, produces a distinctly different surface morphology across all steel types (see Figure 3j–l). The resulting texture is irregular and characterized by circular and cauliflower-like structures.

To obtain a numerical estimation of the uniformity of the surface topography, the isotropy factor can be used. This factor represents the degree of directional uniformity in the texture. In other words, a topography with an isotropy value close to one indicates a topography that is directionally uniform or random, while a value near zero corresponds to a strongly anisotropic texture with clear directional features.<sup>[58]</sup> This is illustrated in **Figure 4a**, which shows the isotropy values as a function of the applied temporal pulse shape (MHz, GHz, Bi-burst, and standard pulsed). In addition, the corresponding  $S_a$  measurements are shown in Figure 4b.

The results show that using MHz (see SEM images in Figure 3d–f), GHz (Figure 3g–i), and Bi-burst (Figure 3j–l) modes produces significantly lower  $S_a$  compared to using no burst (as already discussed in the previous section). The reduction in  $S_a$  with burst modes can be attributed to energy delivery closer to the ablation threshold, resulting in more controlled material removal and reduced overheating.<sup>[35]</sup> Due to the smooth surfaces created by MHz and GHz bursts during layer-by-layer ablation, the direction of the final scanned layer becomes visible. The principal direction of anisotropy is aligned with the scan direction. As a result, the anisotropy introduced by the scanning direction becomes more pronounced despite the overall surface uniformity (Figure 4a).<sup>[57]</sup> Notably, Bi-burst mode achieves high isotropy while maintaining significantly lower  $S_a$  compared to standard pulse ablation, by balancing the effects of heat accumulation and effective ablation.<sup>[37]</sup>

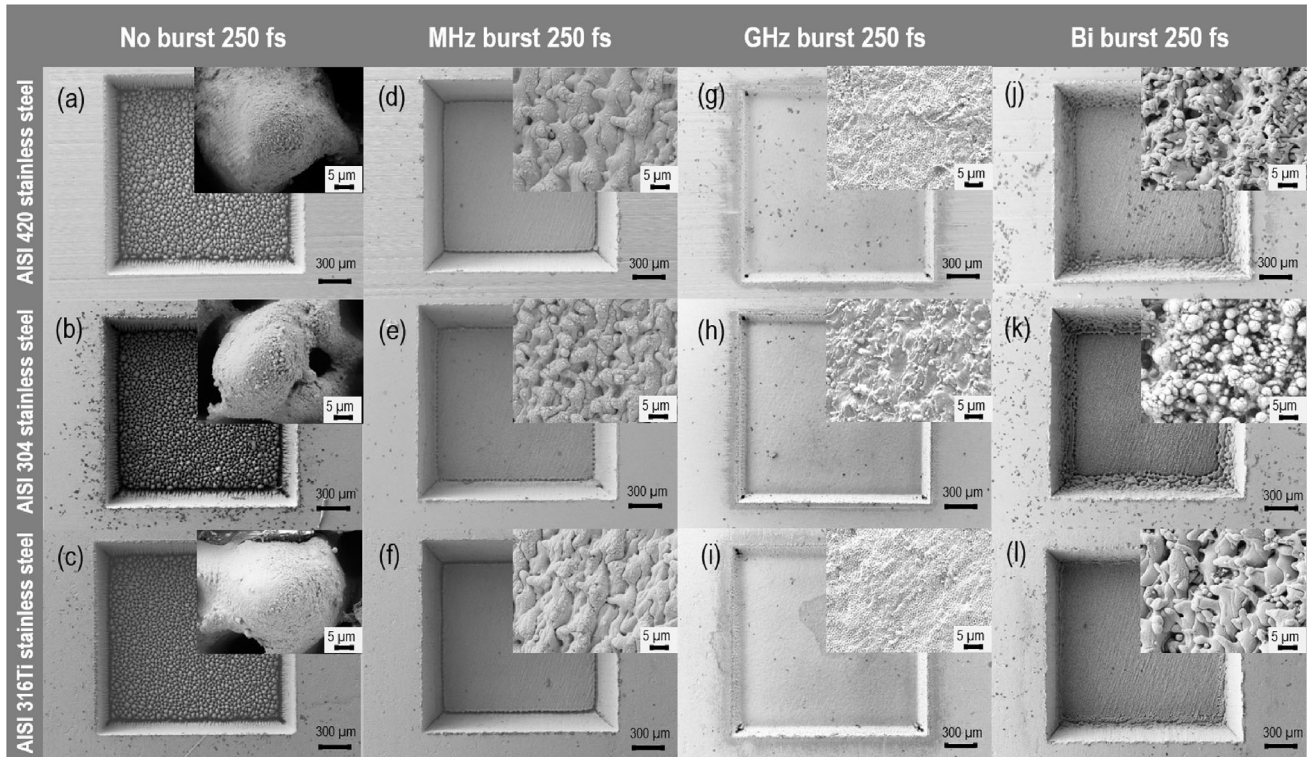


**Figure 3.** SEM images of the laser-treated steel surfaces (AISI 420, AISI 304, and AISI 316Ti) corresponding to the highest reached ablation rates produced by using standard pulsed a–c) no burst and different burst modes d–f) MHz burst; g–i) GHz burst; and j–l) Bi-burst. In all experiments, the following laser parameters were kept constant: fluence at  $\approx 17 \text{ J cm}^{-2}$ , scanning speed at  $3 \text{ m s}^{-1}$ , pulse duration at 250 fs, number of layers at 150 and hatching distance at 5  $\mu\text{m}$ .

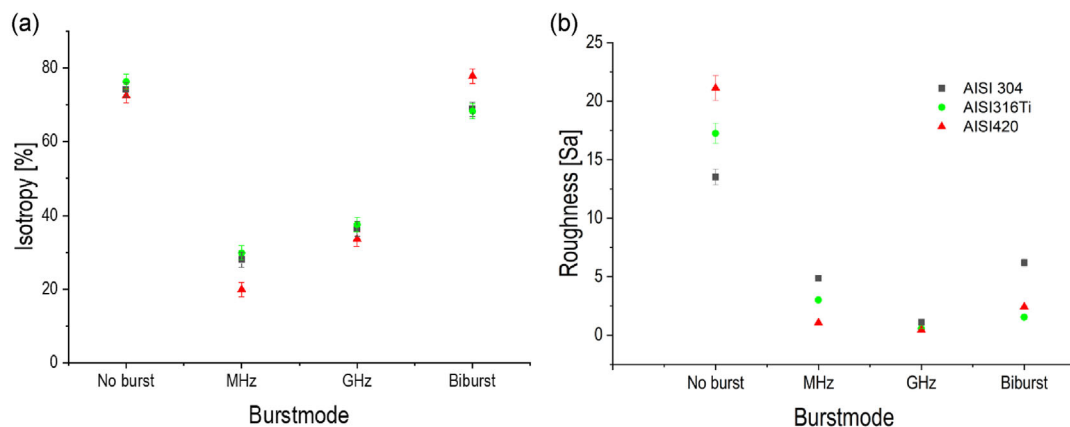


**Figure 4.** a) Isotropy of different surfaces produced by using different burst modes and no burst, and b) the corresponding  $S_a$  for AISI 304, AISI 316Ti, and AISI 420.

Despite a similar  $S_a$  value compared to MHz or GHz bursts, the morphology of the Bi-burst-treated surface is less regular, exhibiting a cauliflower-like structure (see Figure 3j–l). It is assumed that the combination of MHz and GHz bursts results in a more irregular surface morphology due to the interplay between high heat accumulation from the GHz component, which induces partial melting and resolidification, and the high ablation efficiency of the MHz component, which partly ablates the molten layer and hinders uniform resolidification.

While each GHz pulse may induce some ablation, its primary effect is assumed to be thermal, leading to localized heat accumulation and partial surface melting. In this combined configuration, the 10 MHz burst each consists of a sequence of 10 GHz bursts, which collectively benefit from the accumulated heat, thereby enhancing the ablation efficiency and enabling more effective material removal.

On the contrary, using no burst results in increased  $S_a$  and is associated with higher isotropy values and less directionally

**Table 2.** Comparison of the removal rates of different stainless steel alloys using different burst parameters and standard pulsed mode (no burst). In all experiments, following laser parameters were kept constant: fluence at  $\approx 17 \text{ J cm}^{-2}$ , scanning speed at  $3 \text{ m s}^{-1}$ , pulse duration at 250 fs, number of layers at 150 and hatching distance at  $5 \mu\text{m}$ .

Burst mode	No burst		MHz burst		GHz burst		Bi-burst	
	$[\mu\text{m}^3 \mu\text{J}^{-1}]$	$[\text{mm}^3 \text{min}^{-1}]$	$[\mu\text{m}^3 \mu\text{J}^{-1}]$	$[\text{mm}^3 \text{min}^{-1}]$	$[\mu\text{m}^3 \mu\text{J}^{-1}]$	$[\text{mm}^3 \text{min}^{-1}]$	$[\mu\text{m}^3 \mu\text{J}^{-1}]$	$[\text{mm}^3 \text{min}^{-1}]$
AISI 420	1.35	3.23	2.39	5.10	0.32	0.76	1.32	3.16
AISI 304	1.26	3.08	2.28	4.97	0.28	0.69	1.23	2.94
AISI 316Ti	1.27	3.03	2.17	4.47	0.33	0.79	1.32	3.17

structured topographies (see Figure 3a–c). In the case of no burst, the lack of thermal control leads to cumulative surface irregularities that build up layer-by-layer. This means that excessive heat is transferred into the bulk, which negatively affects surface quality. Over multiple layers, the orientation of individual scan paths becomes irrelevant, and the surface texture evolves into a rough and directionally unstructured topography.<sup>[30]</sup> A key observation is that the isotropy trends are consistent across all three tested alloys. This highlights the universal applicability of burst mode tuning for isotropy control.

To better understand the relationship between surface morphology and material removal behavior, the ablation rates for the samples shown in Figure 3 are summarized in Table 2. The data indicate that removal rates for the different burst modes (MHz, GHz, and Bi-burst), as well as for standard pulsed mode,

are similar across all alloys, with a variation of about 7%. However, the choice of temporal pulse shape significantly influences both the removal rate and process efficiency for each alloy.

### 3.3. Defects Produced During the Laser Ablation Processes

#### 3.3.1. Trench Edge Quality

In addition to  $S_a$ , other factors influence the surface quality of laser-ablated trenches. One significant effect is the formation of undesired microholes along the trench edges. Figure 5 shows representative SEM images of the laser-treated area, comparing the effects of different GHz burst modes on the surface morphology, specifically when varying the number of pulses per burst from 3 to 10.

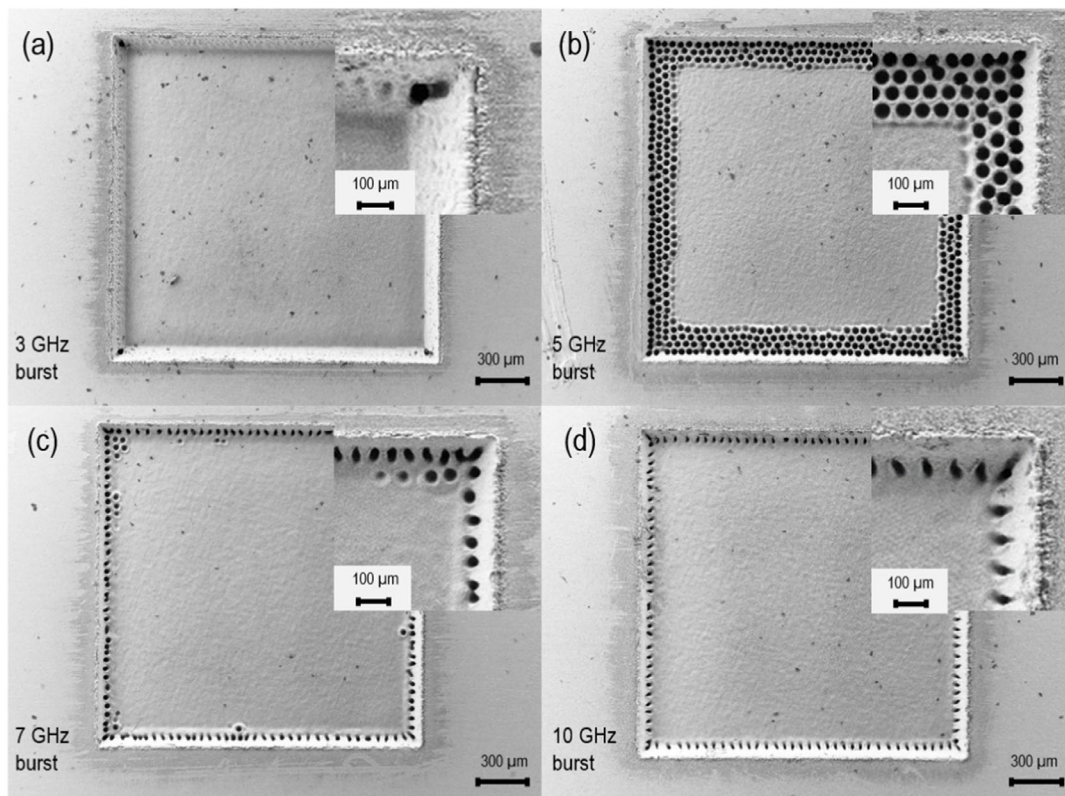


**Figure 5.** Comparison of the surface quality of trenches produced by using GHz burst modes with a) 3, b) 5, c) 7, and d) 10 GHz bursts per pulse on AISI 304 steel. The fluence was kept constant at  $\approx 17 \text{ J cm}^{-2}$ . Images with the same parameters for AISI 420 and AISI 316Ti are depicted in the supplementary material section (Figure S3, Supporting Information).

Interestingly, while the surface quality at the center of the ablated crater remained relatively consistent across these conditions, significant variations emerge along the trench edges. With a three-pulse GHz burst (Figure 5a), a small microhole is visible in each of the four corners of the rectangular-shaped trench. Increasing the number of pulses in the burst to five (Figure 5b) resulted in 3 to 4 rows of evenly distributed microholes surrounding the edge of the laser-treated area.

At seven-pulses per burst (Figure 5c), the number of microholes decreased, forming a single row around the perimeter of the rectangular trench. Additionally, the microholes begin to adopt an elliptical shape. When the number of pulses per burst was increased to 10 (Figure 5 d), a similar distribution of microholes was observed as in the seven-pulse per burst case. However, their elliptical geometry becomes more pronounced and aligned along the trench edges.

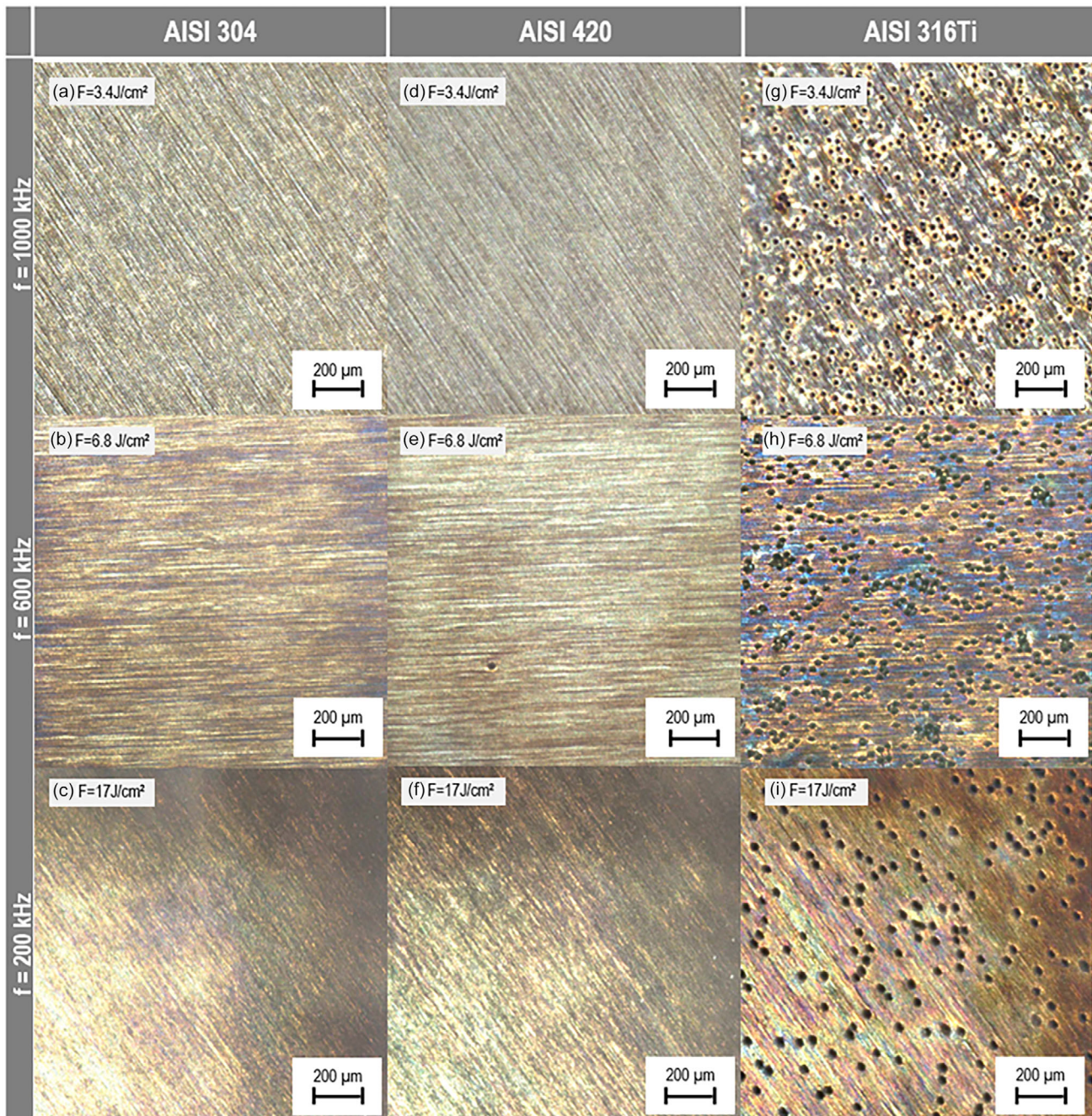


**Figure 6.** Light microscopy images showing the bottom surface of cavities produced using five-pulse GHz bursts with a negative slope in the intraburst energy distribution. Different repetition rates were applied: a,d,g) 200 kHz; b,e,h) 600 kHz; and c,f,i) 1000 kHz, with corresponding variations in fluence. Materials and used fluences are indicated in the figure.

The formation of these microholes is presumed to result from multiple reflections of the laser beam along the tapered edges of the ablated trench. Due to the Gaussian profile of the laser beam, the crater edges develop a taper angle of  $\approx 10^\circ$ . This geometry promotes internal reflections, directing portions of the beam back toward the trench bottom and leading to localized overheating. The resulting heat accumulation causes secondary ablation near the edges, manifesting as microholes.<sup>[59,60–62]</sup>

These findings suggest that microhole formation is a nonlinear phenomenon, influenced by both thermal accumulation and fluid dynamics effects such as the Marangoni flow. Multireflection within the ablation region can lead to the formation of a thin melt layer with a nonuniform thermal distribution. This temperature gradient induces a radial surface tension gradient (Marangoni effect), driving the molten material outward from the hotter beam center toward the cooler periphery and ultimately leading to crater formation upon resolidification.<sup>[58]</sup> A particularly pronounced effect is observed at five-pulses per burst, where the combined influence of these factors is most significant.

### 3.3.2. Influence of Laser Energy Distribution on Surface Quality

To further investigate the influence of laser parameters on surface quality, a series of experiments was conducted focusing on the temporal energy distribution within pulse bursts. In this case, all samples were processed using bursts of five-pulses, with variations in the energy distribution among individual pulses, while maintaining constant average laser power across all test conditions. A negative slope energy profile was applied, meaning that the first pulse in the burst carried the highest energy, and subsequent pulses decreased linearly in energy (slope =  $-1$ ). Additionally, three different pulse repetition rates were tested, being 200, 600, and 1000 kHz.

**Figure 6** shows representative light microscopy images of the laser-treated surfaces for three stainless steel alloys, AISI 304, AISI 420, and AISI 316Ti. For AISI 304 (**Figure 6a–c**), a uniform and homogeneous surface texture was observed across all tested repetition rates, with no noticeable variation in surface morphology. Similarly, for AISI 420 (**Figure 6d–f**), the surface remained consistent across the repetition rates. However, a distinct feature appears at 600 kHz (**Figure 6e**), where a single central microhole was observed within the trench, indicating that while the alloy is not entirely immune to microhole formation, it exhibits almost no susceptibility under all tested conditions.

In contrast, the surfaces of AISI 316Ti (**Figure 6g–i**) exhibit a very high density of microholes across all tested repetition rates, indicating a notably greater propensity for microhole formation in this material.

To better understand the relationship between repetition rate and microhole formation, the number of microholes observed for each material was quantified, as shown in **Figure 7**. As mentioned previously, for AISI 304 and AISI 420 steels, no significant microhole formation was observed across the tested repetition rates, indicating a low susceptibility to defect formation under the given conditions. In contrast, for AISI 316Ti, a clear trend emerges, where an increase in repetition rate leads to a higher number of microholes. This is likely due to the volatilization of molybdenum in this alloy under high laser fluence, which

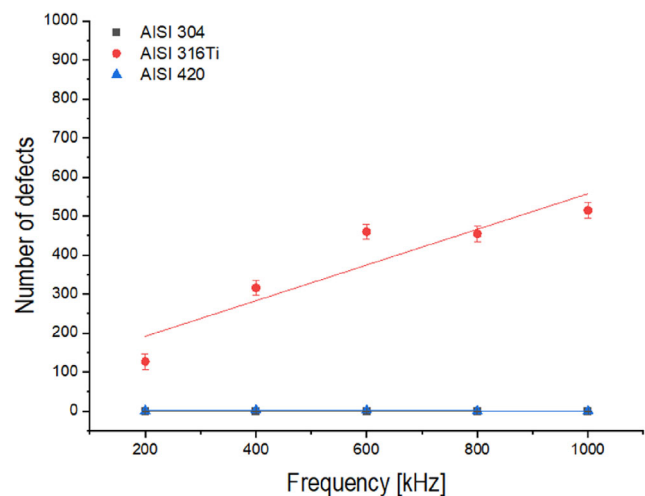


**Figure 7.** Number of microholes formed on the surface of different stainless steel alloys (AISI 304, AISI 420, and AISI 316Ti) as a function of repetition rate, using five-pulse GHz burst mode with a negative energy slope.

disrupts the material's matrix and facilitates microhole formation. At repetition rates in the GHz regime, significant heat accumulation occurs, raising the surface temperature of AISI 316Ti well above its melting point and promoting the vaporization of alloying elements. Regions enriched in molybdenum and titanium may undergo preferential vaporization compared to the surrounding matrix, resulting in localized material loss and void formation. This mechanism likely contributes to the increased susceptibility of AISI 316Ti to microhole defects during GHz burst mode femtosecond laser processing, in contrast to alloys such as AISI 304 or AISI 420. Additionally, the presence of non-metallic inclusions may serve as initiation sites for microhole formation, further exacerbating defect generation under these processing conditions.<sup>[59]</sup>

## 4. Conclusion

In this work, the effects of different burst laser modes (MHz, GHz, and Bi-bursts) on material removal efficiency and surface quality in stainless steel alloys were investigated. A detailed analysis of the postablation surface reveals significant variations in removal rates and surface characteristics across the different laser modes. MHz bursts notably enhance removal rates in high-fluence regimes. For instance, at  $9 \text{ J cm}^{-2}$ , the removal rate could be increased from  $1.5 \text{ mm}^3 \text{ min}^{-1}$  in standard pulsed ablation to  $3.2 \text{ mm}^3 \text{ min}^{-1}$ , more than doubling it compared to standard pulsed ablation.

In contrast, GHz bursts were found to produce very smooth surfaces, with a  $S_a$  of  $\approx 1 \mu\text{m}$  across the tested fluence range. However, this comes at the cost of ablation efficiency. At a fluence of  $9 \text{ J cm}^{-2}$ , the ablation efficiency dropped significantly to  $0.32 \mu\text{m}^3 \mu\text{J}^{-1}$  for GHz bursts, compared to  $1.35 \mu\text{m}^3 \mu\text{J}^{-1}$  for standard pulsed ablation and  $2.6 \mu\text{m}^3 \mu\text{J}^{-1}$  for MHz bursts. Bi-bursts, which combine MHz and GHz components, were shown to offer a versatile approach for balancing removal rates, removal efficiency, and surface quality. Depending on the used temporal

configuration, removal volumes comparable to those of standard pulsed ablation were achieved, reaching  $\approx 3.2 \text{ mm}^3 \text{ min}^{-1}$  at  $17 \text{ J cm}^{-2}$ . In addition, the removal efficiency was enhanced by increasing the proportion of MHz pulses, whereas a higher share of GHz pulses led to improved surface quality.  $S_a$  obtained with Bi-bursts was generally lower than in standard pulsed ablation at high fluences but tended to increase linearly above  $6 \text{ J cm}^{-2}$ , reaching values between those observed with MHz and GHz bursts alone.

Additionally, the alloy type and the energy distribution within the pulse train played significant roles in microhole formation and overall ablation quality, while the precise role of intraburst energy distribution effects remains an open question for further investigation.

## Supporting Information

Supporting Information is available from the Wiley Online Library or from the author.

## Acknowledgements

D.O. acknowledges the financial support of KSF Institute as well as the DFG (grant 505067193), for financing the SEM Microscope. The support of the project partner GF Machining Solutions GmbH and Lightconversion UAB is also acknowledged.

Open Access funding enabled and organized by Projekt DEAL.

## Conflict of Interest

The authors declare no conflict of interest.

## Data Availability Statement

The data that support the findings of this study are available in the supplementary material of this article.

## Keywords

burst ablation, burst modes, stainless steels, thermal diffusivities, ultrashort pulsed lasers, volume ablation

Received: May 5, 2025  
Revised: September 5, 2025  
Published online:

- [1] R. J. Narayan, *Materials for Medical Devices*, ASM International, Materials Park, OH **2012**, pp. 199–210.
- [2] D. A. K. Patel, *J. Mater. Sci. Eng.* **2015**, *5*, 4.
- [3] J. Manfredi, *Filtration and Purification in The Biopharmaceutical Industry*, CRC Press, Boca Raton, FL **2019**.
- [4] Y. Xu, Y. Li, T. Chen, C. Dong, K. Zhang, X. Bao, *J. Mater. Res. Technol.* **2024**, *29*, 2788.
- [5] V. Geantă, I. Voiculescu, R. Stefanioiu, E. R. Rusu, *Key Eng. Mater.* **2013**, *583*, 9.
- [6] K. Walley, M. Bajraliu, T. Gonzalez, A. Nazarian, *Orthop. J. Harvard Med. Sch.* **2016**, *17*, 68.

- [7] G. L. Winters, M. J. Nutt, *Stainless Steels For Medical And Surgical Applications*, ASTM International, West Conshohocken, PA **2003**.
- [8] L. Reclaru, R. Ziegenhagen, P.-Y. Eschler, A. Blatter, J. Lemaître, *Acta Biomater.* **2006**, *2*, 433.
- [9] J. R. Deepak, A. R. P., S. Saran Sundar, *Mater. Today: Proc.* **2023**.
- [10] M. Alsaadawy, M. Dewidar, A. Said, I. Maher, T. A. Shehabeldeen, *Int. J. Adv. Manuf. Technol.* **2024**, *130*, 1039.
- [11] A. Klimpel, *Materials* **2024**, *18*, 17.
- [12] A. Gruner, J. Schille, U. Loeschner, *J. Laser Micro/Nanoeng.* **2024**, *19*, 20.
- [13] N. Ackerl, P. Gugger, K. Wegener, *J. Laser Appl.* **2020**, *32*, 032013.
- [14] R. Mahesh, A. Senthilkumar, G. Antony Casmir Jayaseelan, K. Sooraj, P. Sayooj, A. M. Punnoose, *Advancements in Materials Processing Technology*, Vol. 58 (Eds: R. Sahu, R. Krishna, R. Prasad), Springer Nature Singapore, Singapore **2024**, p. 213.
- [15] B. Rethfeld, D. S. Ivanov, M. E. Garcia, S. I. Anisimov, *J. Phys. D: Appl. Phys.* **2017**, *50*, 193001.
- [16] M. E. Povarnitsyn, V. B. Fokin, P. R. Levashov, T. E. Itina, *Phys. Rev. B* **2015**, *17*, 92.
- [17] M. Park, Y. Gu, X. Mao, C. P. Grigoropoulos, V. Zorba, *Sci. Adv.* **2023**, *9*, eadf6397.
- [18] A. Amouye Foumani, D. J. Förster, H. Ghorbanfekr, R. Weber, T. Graf, A. R. Niknam, *Appl. Surf. Sci.* **2021**, *537*, 147775.
- [19] C. Chen, M. Spellaugue, D. Redka, R. Auer, C. Doñate-Buendia, S. Barcikowski, B. Gökce, H. P. Huber, L. V. Zhigilei, *Phys. Rev. B* **2025**, *17*, 111.
- [20] B. Neuenschwander, T. Kramer, B. Lauer, B. Jaeggi, *Laser Applications in Microelectronic And Optoelectronic Manufacturing (LAMOM) XX* (Eds: S. Roth, Y. Nakata, B. Neuenschwander, X. Xu), SPIE, Bellingham, WA **2015**, p. 93500U.
- [21] B. Neuenschwander, B. Jaeggi, M. Zimmermann, V. Markovic, B. Resan, K. Weingarten, R. de Loor, L. Penning, *J. Laser Appl.* **2016**, *28*, 022506.
- [22] J. Schille, L. Schneider, U. Loeschner, *Appl. Phys. A* **2015**, *120*, 847.
- [23] A. Žemaitis, P. Gečys, M. Barkauskas, G. Račiukaitis, M. Gedvilas, *Sci. Rep.* **2019**, *9*, 1.
- [24] B. Jaeggi, S. Remund, R. Streubel, B. Goekce, S. Barcikowski, B. Neuenschwander, *J. Laser Micro/Nanoeng.* **2017**, *3*, 12.
- [25] B. Neuenschwander, B. Jaeggi, D. J. Förster, T. Kramer, S. M. Remund, *J. Laser Appl.* **2019**, *31*, 1.
- [26] A. Žemaitis, M. Gaidys, J. Mikšys, P. Gečys, M. Gedvilas, *Laser Applications In Microelectronic And Optoelectronic Manufacturing (LAMOM) XXVI Vol. 11673* (Eds: C. Molpeceres, A. Narazaki, J. Qiao), SPIE, Bellingham, WA **2021**, p. 26.
- [27] T. Hirsiger, M. Gafner, S. M. Remund, M. Chaja, A. Urniežius, S. Butkus, B. Neuenschwander, *Laser Applications In Microelectronic And Optoelectronic Manufacturing (LAMOM) XXV* (Eds: G. Račiukaitis, C. Molpeceres, A. Narazaki, J. Qiao), SPIE, Bellingham, WA **2020**, p. 27.
- [28] M. Sailer, F. Bauer, J. Kleiner, M. Kaiser, *Laser Inst. Am.* **2015**.
- [29] J. Schille, L. Schneider, U. Loeschner, R. Ebert, P. Scully, N. Goddard, B. Steiger, H. Exner, *ICALEO* **2011**, 773.
- [30] H. Le, T. Karkantonis, V. Nasrollahi, P. Penchev, S. Dimov, *Appl. Phys. A* **2022**, *128*, 1.
- [31] A. Žemaitis, M. Gaidys, P. Gečys, M. Barkauskas, M. Gedvilas, *Opt. Express* **2021**, *29*, 7641.
- [32] S. M. Remund, M. Gafner, M. Chaja, A. Urniežius, S. Butkus, B. Neuenschwander, *Procedia CIRP* **2020**, *94*, 850.
- [33] A. Žemaitis, M. Gaidys, P. Gečys, M. Gedvilas, *Sci. Rep.* **2024**, *14*, 5614.
- [34] P. Lickschat, D. Metzner, S. Weißmantel, *J. Laser Appl.* **2021**, *33*, 022005.

- [35] D. J. Förster, S. Faas, S. Gröninger, F. Bauer, A. Michalowski, R. Weber, T. Graf, *Appl. Surf. Sci.* **2018**, *440*, 926.
- [36] D. Redka, M. Spellauge, C. Sandner, J. Minár, H. P. Huber, *Appl. Surf. Sci.* **2025**, *686*, 162190.
- [37] M. Gaidys, A. Žemaitis, P. Gečys, M. Gedvilas, *RSC Adv.* **2023**, *13*, 3586.
- [38] D. Obergfell, B. Azarhoushang, A. F. Lasagni, *Mater. Lett.* **2024**, *365*, 1.
- [39] D. Obergfell, B. Azarhoushang, A. F. Lasagni, *Adv. Eng. Mater.* **2023**, *25*, 1.
- [40] F. Bauer, *J. Laser Micro/Nanoeng.* **2015**, *10*, 325.
- [41] D. J. Förster, B. Jaeggi, A. Michalowski, B. Neuenschwander, *Materials* **2021**, *14*, 1.
- [42] C. Kerse, H. Kalaycıoğlu, P. Elahi, B. Çetin, D. K. Kesim, Ö. Akçaalan, S. Yavaş, M. D. Aşık, B. Öktem, H. Hoogland, R. Holzwarth, F. Ö. Ilday, *Nature* **2016**, *537*, 84.
- [43] E. Audouard, E. Mottay, *Int. J. Extrem. Manuf.* **2023**, *5*, 1.
- [44] J. Lopez, S. Niane, G. Bonamis, E. Audouard, C. Hönninger, E. Mottay, I. Manek-Hönninger, *Int. J. Extrem. Manuf.* **2022**, *11988*, 6.
- [45] G. Bonamis, E. Audouard, C. Hönninger, J. Lopez, K. Mishchik, E. Mottay, I. Manek-Hönninger, *Opt. Express* **2020**, *28*, 27702.
- [46] P. Balage, M. Lafargue, T. Guilberteau, G. Bonamis, C. Hönninger, J. Lopez, I. Manek-Hönninger, *Micromachines* **2023**, *9*, 14.
- [47] P. Balage, M. Lafargue, T. Guilberteau, G. Bonamis, C. Hönninger, J. Lopez, I. Manek-Hönninger, *Micromachines* **2024**, *15*, 632.
- [48] Z. Lin, L. V. Zhigilei, V. Celli, *Phys. Rev. B* **2008**, *7*, 77.
- [49] D. S. Ivanov, L. V. Zhigilei, *Phys. Rev. B* **2003**, *6*, 68.
- [50] M. V. Shugaev, C. Wu, O. Armbruster, A. Naghilou, N. Brouwer, D. S. Ivanov, T. J.-Y. Derrien, N. M. Bulgakova, W. Kautek, B. Rethfeld, L. V. Zhigilei, *MRS Bull.* **2016**, *41*, 960.
- [51] J. Schille, L. Schneider, A. Streek, S. Kloetzer, U. Loeschner, *Opt. Eng.* **2016**, *55*, 096109.
- [52] F. Schell, C. Zwahr, A. F. Lasagni, *Nanomaterials* **2024**, *13*, 14.
- [53] X. Li, Y. Guan, *Nanotechnol. Precis. Eng.* **2020**, *3*, 105.
- [54] S.-A. Anghel, M. Oane, C. N. Mihăilescu, B. A. Sava, M. Elişa, N. Mihăilescu, D. Ticoş, A. M. I. Trefilov, C. Ristoscu, A. V. Filip, I. N. Mihăilescu, *Metals* **2023**, *13*, 1775.
- [55] B. Neuenschwander, B. Jaeggi, E. V. Zavedeev, N. R. Arutyunyan, S. M. Pimenov, *J. Appl. Phys.* **2019**, *11*, 126.
- [56] A. Žemaitis, M. Gaidys, P. Gečys, M. Barkauskas, M. Gedvilas, *Optics Express* **2020**, *29*, 7641.
- [57] D. Metzner, P. Lickschat, S. Weißmantel, *Appl. Surf. Sci.* **2020**, *531*, 147270.
- [58] W. D. Callister, D. G. Rethwisch, *Materials Science and Engineering: An Introduction SI Version*, Wiley, Hoboken **2020**.
- [59] G. Schnell, H. Lund, S. Bartling, C. Polley, A. Riaz, V. Senz, A. Springer, H. Seitz, *Appl. Surf. Sci.* **2021**, *570*, 151115.
- [60] T. Barthels, M. Niessen, C. Heinigk, *Opt. Eng.* **2022**, *12*, 61.
- [61] H. Liu, W. Lin, Z. Lin, L. Ji, M. Hong, *Adv. Funct. Mater.* **2019**, *42*, 29.
- [62] N. Zamora-Romero, M. A. Camacho-Lopez, M. Camacho-Lopez, A. R. Vilchis-Nestor, V. H. Castrejon-Sanchez, S. Camacho-Lopez, G. Aguilar, *J. Alloys Compd.* **2019**, *788*, 666.